AGU PUBLICATIONS

JGR

Journal of Geophysical Research: Earth Surface

RESEARCH ARTICLE
10.1002/2017JF004329

Key Points:
- Moffatt eddies likely form and disrupt stratigraphy at the base of ice sheets
- Observed deep valleys in Gamburtsev Subglacial Mountains likely produce eddies
- Eddies likely contaminate climate records in ice cores

Correspondence to:
C. R. Meyer,
colinrmeyer@gmail.com

Citation:
Meyer, C. R., and T. T. Creyts (2017), Formation of ice eddies in subglacial mountain valleys, *J. Geophys. Res. Earth Surf.*, *122*, 1574–1588, doi:10.1002/2017JF004329.

Received 20 APR 2017
Accepted 27 JUL 2017
Accepted article online 11 AUG 2017
Published online 5 SEP 2017

Formation of ice eddies in subglacial mountain valleys

Colin R. Meyer[1] **and Timothy T. Creyts**[2]

[1]John A. Paulson School of Engineering and Applied Sciences, Harvard University, Cambridge, Massachusetts, USA, [2]Lamont-Doherty Earth Observatory, Columbia University, New York, New York, USA

Abstract Radar data from both Greenland and Antarctica show folds and other disruptions to the stratigraphy of the deep ice. The mechanisms by which stratigraphy deforms are related to the interplay between ice flow and topography. Here we show that when ice flows across valleys or overdeepenings, viscous overturnings called Moffatt eddies can develop. At the base of a subglacial valley, the shear on the valley sidewalls is transferred through the ice, forcing the ice to overturn. To understand the formation of these eddies, we numerically solve the non-Newtonian Stokes equations with a Glen's law rheology to determine the critical valley angle for the eddies to form. When temperature is incorporated into the ice rheology, the warmer basal ice is less viscous and eddies form in larger valley angles (shallower slopes) than in isothermal ice. We also show that when ice flow is not perpendicular to the valley orientation, complex 3-D eddies transport ice down the valley. We apply our simulations to the Gamburtsev Subglacial Mountains and solve for the ice flow over radar-determined topography. These simulations show Moffatt eddies on the order of 100 m tall in the deep subglacial valleys.

1. Introduction

Observations of mismatched stratigraphy and overturning in ice cores highlight the relationship between ice flow and topography [*Grootes et al.*, 1993; *Jacobel and Hodge*, 1995; *Dahl-Jensen et al.*, 2013]. Stratigraphic disturbances result from a variety of fluid dynamical mechanisms. For example, ice flowing over a flat bed can fold due to transitions in basal slip conditions, whereby variation in the downstream velocity over a transition in basal slip is accommodated by an increase in vertical velocity [*Weertman*, 1976; *Wolovick et al.*, 2014]. Folds can also occur by viscous buckling [e.g., *Hudleston and Stephansson*, 1973], ice crystal anisotropy [*Alley et al.*, 1997], transient flow over an undulatory bed [*Hudleston*, 1976; *Waddington et al.*, 2001], or slip along internal layers indicating a breakdown in fluid rheology [*Whillans and Jezek*, 1987].

These disturbances are commonly found near the bed rendering that ice difficult to date and interpret. Simultaneously, these deep layers contain the oldest climate archive [*Van Liefferinge and Pattyn*, 2013]. Presently, all deep cores have disrupted stratigraphy near the base, e.g., NGRIP/GISP2/EPICA DomeC/Vostok/Dye3 [*Dahl-Jensen et al.*, 2013]. Whether these disruptions form in situ or migrate great distances is of critical importance to estimate the extent of disruptions. Understanding the physics of the base of the ice sheet and its effects on deep ice is therefore of necessary to estimate the location of pristine ice from models. Additionally, modeled streamlines inform interpretations of layered stratigraphy determined from ice-penetrating radar. Understanding the formation, localization, and migration of stratigraphic disturbances will lead to a better assessment of deep climate archives.

Mechanisms for overturning are driven by variation in topography. *Gudmundsson* [1997] analyzed ice sliding over sinusoidal basal topography to determine affect of the frequency and amplitude of the sinusoidal topography on velocity structure within the ice. For a sufficiently undulatory bed, characterized by a sinusoidal amplitude-to-wavelength ratio of 0.28, *Gudmundsson* [1997] numerically observed overturning streamlines in the sinusoid troughs called Moffatt eddies. *Moffatt* [1964a, 1964b] derived the conditions under which a Newtonian fluid flowing at low Reynolds number deep in a corner can form an eddy. Specifically, Moffatt determined the critical angle of the corner required to form an eddy. *Fenner* [1975] and *Henriksen and Hassager* [1989] extended Moffatt's calculation to non-Newtonian fluids and determined that the critical angle as a function of the rheological parameters.

In this manuscript, we show that Moffatt eddies can form when ice flows over sufficiently steep valleys. In the first section, we describe the character of these eddies and the conditions under which they form. We then

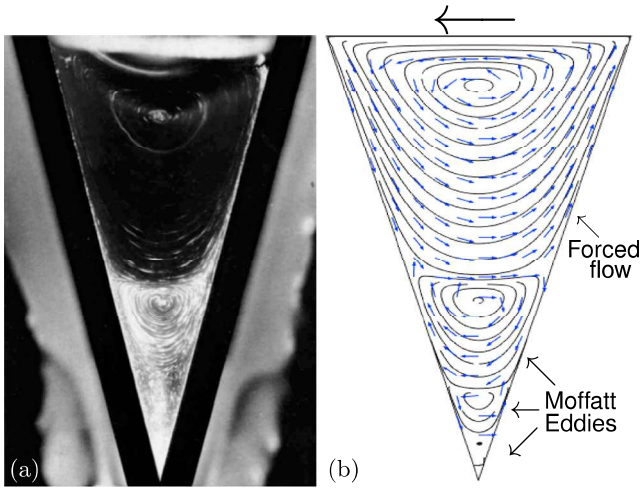

Figure 1. (a) Moffatt eddies in a Newtonian fluid: experimental visualization from *Taneda* [1979]. (b) Schematic streamlines showing the sequence of Moffatt eddies.

use numerical simulations to analyze the flow of temperature-dependent ice over model valleys. In the last section, we apply the numerical simulations to flow of ice over subglacial valleys in the Gamburtsev Subglacial Mountains and compare our simulations to published radar data.

1.1. Moffatt Eddies in a Newtonian Fluid

Moffatt eddies are recirculation zones that occur as a very viscous fluid flows over a sharp corner [*Moffatt*, 1964a, 1964b; *Acheson*, 1990]. Figure 1a shows an experiment using a slowly rotated cylinder on top of a wedge filled with highly viscous glycerin oil [*Taneda*, 1979], and Figure 1b is a schematic simulation. The top part of the fluid spins in contact with the cylinder, while deep in the corner the streamlines separate and Moffatt eddies form. The forced flow only acts as a far-field driver, and Moffatt eddies form due to a difference in shear as the boundary conditions on the sides of the wedge interact. The streamlines in Figure 1b show that the primary eddy visible in the experiment is only the first eddy in a sequence of eddies of decaying amplitudes. The velocity vectors in the schematic show that the direction of rotation alternates along the sequence.

To analyze the formation of Moffatt eddies, we consider the two-dimensional Stokes flow of a Newtonian fluid in a wedge (Figure 2), which is governed by the biharmonic equation for the stream function ψ

$$\nabla^4 \psi = 0.$$

Moffatt [1964a] shows that this equation admits a set of similarity solutions of the form

$$\psi = r^{\lambda} f(\theta),$$

where r represents the radial distance from the corner and θ is the angle. This similarity solution is a class of coupled separable solutions where the function $f(\theta)$ depends on an unknown radial exponent λ. Thus, as part of the solution for $f(\theta)$, we must also determine the value of λ. At a critically small wedge opening angle of $\alpha_c = 146.3°$, the exponent λ becomes complex, i.e., $\lambda = \lambda_R + i\lambda_I$ (cf. Figure 3). The consequence of a complex exponent is that the horizontal velocity will alternate in sign along r, e.g., at $\theta = \alpha/2$,

$$u \sim r^{\lambda_R - 1} e^{i(\lambda_I - 1)\ln(r)}, \qquad (1)$$

where u is the horizontal velocity, cf. equation (6). That is, the switch from a real to a complex exponent indicates a switch from a unidirectional flow to a flow in which the horizontal velocity alternates in sign: the streamlines disconnect from the bulk flow and connect with lower streamlines, forming eddies (Figure 1). In this way, these eddies are a consequence of the no-slip boundary conditions on either side of the wedge communicating through the fluid. Mathematically,

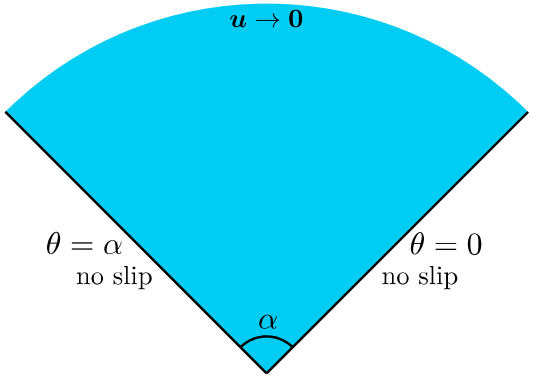

Figure 2. Two-dimensional wedge domain with opening angle α. The interior of the wedge is filled with a power law fluid with exponent $n = 1$ for Newtonian fluid and $n = 3$ for Glen's law for a subglacial valley.

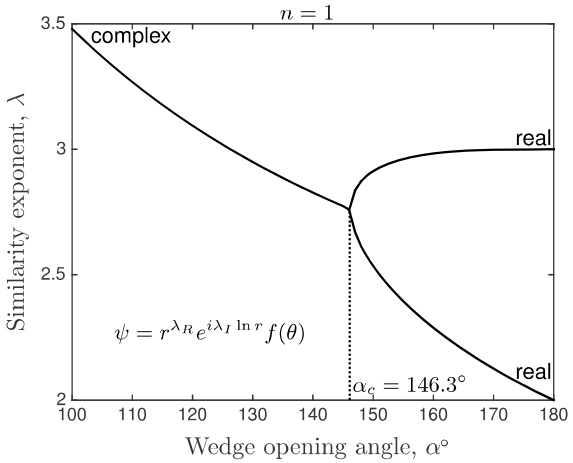

Figure 3. Similarity exponent λ dependence on wedge angle α for $n = 1$ [*Moffatt*, 1964a, 1964b; *Acheson*, 1990]. The critical corner angle α_c occurs at the transition between real and complex λ shown by the dotted line. A qualitatively similar transition can be found for all n.

there is an infinite sequence of these eddies, i.e., $\ln(r) \to \infty$ as $r \to 0$ in equation (1), although their successive amplitude decays exponentially. Only the first eddy in the sequence is visible in the experiment by *Taneda* [1979], Figure 1a, as the scale of the smaller eddies is limited by the viscosity and the passive tracer used for imaging.

1.2. Moffatt Eddies in Ice

We now describe Moffatt eddies in ice, where the non-Newtonian rheology of ice leads to subtle differences between Moffatt eddies in ice and in a Newtonian fluid. The creep of ice over long periods of time is that of a viscous fluid with a non-Newtonian rheology. It is common in glaciology to use a shear-thinning power law rheology called Glen's law [*Glen*, 1955; *Cuffey and Paterson*, 2010]

$$\dot{\epsilon}_E = A(T)\tau_E^n, \tag{2}$$

where $A(T)$ is the ice softness ($\mathrm{Pa}^{-n}\ \mathrm{s}^{-1}$) as a function of temperature T (section 2.1) and

$$\tau_E = \sqrt{\frac{1}{2}\tau_{ij}\tau_{ij}} \quad \text{and} \quad \dot{\epsilon}_E = \sqrt{\frac{1}{2}\dot{\epsilon}_{ij}\dot{\epsilon}_{ij}}$$

are the second invariants of the deviatoric stress

$$\tau_{ij} = \sigma_{ij} + p\delta_{ij}$$

and strain rate

$$\dot{\epsilon}_{ij} = \frac{1}{2}\left(\frac{\partial u_i}{\partial x_j} + \frac{\partial u_j}{\partial x_i}\right), \tag{3}$$

tensors, respectively. The parameter n is the rheological exponent, where values of n greater than unity indicate a decreasing effective viscosity with increased shear, i.e., a shear-thinning rheology. In glaciology, n can vary from $n = 1$ to 4 but is typically chosen to be 3 [*Durham et al.*, 1997; *Goldsby and Kohlstedt*, 2001; *Cuffey and Paterson*, 2010]. In a power law fluid, the critical angle α_c for the formation of Moffatt eddies depends on the rheological exponent n [*Fenner*, 1975; *Henriksen and Hassager*, 1989].

The onset of recirculation for a Newtonian fluid flowing across a wedge is governed by a critical wedge angle α_c, Figure 3. For a fluid with a power law rheology, we aim to determine how the critical angle α_c depends on the rheological exponent n. To this end, we derive a similarity solution for corner eddies that form in slow viscous power law fluids [*Fenner*, 1975; *Henriksen and Hassager*, 1989]. The momentum and mass conservation equations for a two-dimensional incompressible flow are given as

$$\nabla \cdot \boldsymbol{\sigma} = 0 \quad \text{and} \quad \nabla \cdot \boldsymbol{u} = 0.$$

Taking the curl of the momentum equation, using mass conservation, and writing the result in polar coordinates, we obtain

$$2\frac{\partial}{\partial\theta}\left[\frac{\tau_{rr}}{r} + \frac{\partial\tau_{rr}}{\partial r}\right] + \frac{1}{r}\frac{\partial^2\tau_{r\theta}}{\partial\theta^2} - 3\frac{\partial\tau_{r\theta}}{\partial r} - r\frac{\partial^2\tau_{r\theta}}{\partial r^2} = 0. \tag{4}$$

Using Glen's law from equation (2), we can relate the deviatoric stress to the strain rates as

$$\tau_{ij} = A^{-1/n}\dot{\epsilon}_E^{(1-n)/n}\dot{\epsilon}_{ij}. \tag{5}$$

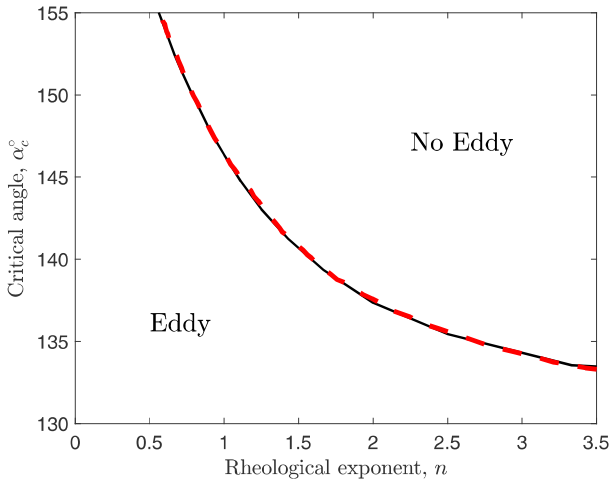

Figure 4. Critical corner angle α_c in degrees for which eddies first appear as a function of the rheological exponent n. The red dashed line is modified from the computational results of *Henriksen and Hassager* [1989].

The strain rates are derivatives of the velocity (equation (3), and, by definition, the velocity can be written in terms of the stream function as

$$u_r = -\frac{1}{r}\frac{\partial \psi}{\partial \theta} \quad \text{and} \quad u_\theta = \frac{\partial \psi}{\partial r}. \tag{6}$$

Because each term in equation (4) scales as $1/r$, we can write the stream function as

$$\psi = r^\lambda f(\theta), \tag{7}$$

which is the leading order term and only valid asymptotically close to the corner, i.e., $r \ll d_c$, where d_c is the depth of the wedge. Inserting this form for the stream function into the momentum balance, equation (4), using equations (5) and (6) gives

$$\begin{aligned} &4(\lambda-1)\left[(\lambda-2)+n\right]\left(\frac{1-n}{2}\Gamma\Gamma' f' + n\Gamma^2 f''\right) \\ &-\frac{1-n}{2}\left(\frac{1-3n}{2}(\Gamma')^2 + n\Gamma\Gamma''\right)\left[\lambda(\lambda-2)f - f''\right] \\ &-(n-n^2)\Gamma\Gamma'\left[\lambda(\lambda-2)f' - f'''\right] - \Gamma^2\left[\lambda(\lambda-2)f'' - f^{iv}\right] \\ &+(\lambda-2)\left[(\lambda-2)+2n\right]\Gamma^2\left[\lambda(\lambda-2)f - f''\right] = 0, \end{aligned} \tag{8}$$

where Γ is given as

$$\Gamma = \left[2(1-\lambda)f'\right]^2 + \left[\lambda(\lambda-2)f - f''\right]^2.$$

We apply no-slip boundary conditions on the sides of the wedge:

$$f(0) = f(\alpha) = 0 \quad \text{and} \quad f'(0) = f'(\alpha) = 0. \tag{9}$$

In this paper, we use no slip in order to understand the basic physics of the formation of eddies. Our results apply broadly to the interior of the ice sheet where the ice at the bed flows slowly. These areas flow chiefly by internal deformation of ice constrained by basal stress, which is well approximated by no-slip conditions, i.e., the depth of the valley is much greater than the slip length. In glaciology, sliding is parametrized by a sliding law for the basal boundary condition and the empirical coefficients in these laws may not be physically justifiable [*Weertman*, 1957; *Lliboutry*, 1968; *Schoof*, 2005]. However, such sliding may be important in areas of fast flow such as ice streams, which typically have low topographic relief. Additionally, there can be localized slip over small subglacial lakes in the bottom of valleys as discussed later in section 4.3. If a sliding law is imposed, then a similarity solution of the from in equation (7) does not exist, and the semianalytical method described here will not work. We leave the investigation of sliding for future work.

The similarity ordinary differential equation for $f(\theta)$ in equation (8) is equidimensional in f and, therefore, indeterminate up to a multiplying constant. We impose an additional condition equation (8) to normalize the stress along the sides of the wedge as

$$f''(0) = 1,$$

which specifies a single eigenvalue λ [*Henriksen and Hassager*, 1989].

We solve equation (8) numerically using a shooting method [*Hutchinson*, 1968; *Fenner*, 1975; *Henriksen and Hassager*, 1989]. We vary the value of $f'''(0)$ until the boundary conditions on $\theta = \alpha$ are satisfied while simultaneously solving for λ using the extra condition on $\theta = 0$. For each value of the rheological exponent n, we use this shooting method to determine the exponent λ at angles between 100° and 180°. Thus, we find the critical angle α_c at which λ becomes complex (e.g., the transition in Figure 3) as a function of n. Figure 4 shows α_c as a function of n and compares our results to a modified version of Figure 7 in *Henriksen and Hassager* [1989]. This curve marks the boundary between eddies forming or not. For a given rheological exponent, valleys with opening angles below the line will form eddies and valleys with angles above the line will not.

Moffatt eddies form due to a difference in shear as the boundary conditions on the sides of the wedge interact. Figure 4 shows that $\alpha_c = 134°$, which is slightly less than the value for a Newtonian fluid, and therefore requires steeper wedge sides to form Moffatt eddies. Larger values of n increase the degree of shear thinning, and shear more easily localizes and does not propagate as far into the fluid. Therefore, the opening angle of the wedge must decrease in order for the shear on each edge of the wedge to interact as n increases.

2. Analysis

Here we model the flow of ice over model valleys using finite element numerical solutions. We solve for the ice velocity and ice temperature, which are coupled through the ice viscosity, softening the ice where it is warm and hardening the ice in cold regions. From the velocity field, we compute the streamlines and observe Moffatt eddies in locations where the streamlines recirculate. For our computations we use the preexisting finite element package COMSOL Multiphysics [*COMSOL*, 2006]. Before describing the simulation results, we outline the coupled ice-temperature equations and their respective boundary conditions.

2.1. Temperature-Dependent Viscosity

The ice softness A from Glen's law, equation (2), is strongly temperature dependent and commonly modeled as an Arrhenius function [*Cuffey and Paterson*, 2010]

$$A = A_0 e^{-(Q_c/RT)[1-(T/T^*)]}, \tag{10}$$

where A_0 is the ice softness prefactor, Q_c is the activation energy per mole of ice, $R = 8.314\ \mathrm{J\,K^{-1}\,mol^{-1}}$ is the ideal gas constant, T is the ice temperature (ignoring the small effect of pressure melting), and $T^* = 263.15\ \mathrm{K}$ is the transition temperature where the activation energy Q_c changes slope due to premelting along grain boundaries, i.e.,

$$Q_c = \begin{cases} 60\ \mathrm{kJ/mol}, & T < 263.15\ \mathrm{K} \\ 115\ \mathrm{kJ/mol}, & T > 263.15\ \mathrm{K} \end{cases}.$$

We nondimensionalize the variables as

$$\boldsymbol{u} = u_s \hat{\boldsymbol{u}}, \boldsymbol{x} = H\hat{\boldsymbol{x}}, \dot{\epsilon} = \frac{u_s}{H}\hat{\epsilon}, \boldsymbol{\nabla} = \frac{1}{H}\hat{\boldsymbol{\nabla}},$$
$$A = A_0 \hat{A}\left(\hat{T}\right), p = p_0 \hat{p}, k = k_0 \hat{k}\left(\hat{T}\right), T = T^* \hat{T},$$

where u_s is the surface velocity of the ice and H is the ice thickness (Table 1). Inserting these scalings into the ice softness function and dropping the hats, we have

$$A(T) = e^{\Pi(T)[1-(1/T)]} \quad \text{with} \quad \Pi(T) = \begin{cases} 27.4, & T < 1 \\ 52.6, & T > 1 \end{cases}.$$

Based on the other parameters, we choose the pressure to scale as

$$p_0 = A_0^{-1/n}\left(\frac{u_s}{H}\right)^{\frac{1}{n}},$$

which is the Glen's law version of the slow viscous pressure scale $\mu u_s/H$.

2.2. Nondimensional Governing Equations

The nondimensional equations for the balances of internal energy, momentum, and mass are

$$\mathrm{Pe}\boldsymbol{u}\cdot\boldsymbol{\nabla}T = \boldsymbol{\nabla}\cdot(k\boldsymbol{\nabla}T) + \mathrm{Br}A^{-\frac{1}{n}}\dot{\epsilon}_E^{\frac{1}{n}+1},$$
$$\boldsymbol{\nabla}\cdot\left(A^{-\frac{1}{n}}\dot{\epsilon}_E^{\frac{1}{n}-1}\dot{\epsilon}\right) = \boldsymbol{\nabla}p,$$
$$\boldsymbol{\nabla}\cdot\boldsymbol{u} = 0,$$

Table 1. Parameters for Ice From *Cuffey and Paterson* [2010] and Parameters Representative of the Gamburtsev Subglacial Mountains [*Bell and othes*, 2011; *Rignot et al.*, 2011; *Creyts et al.*, 2014][a]

ρ	900	(kg m^{-3})	Ice density
c_p	$153 + 1870T$	(J kg^{-1} K^{-1})	Specific heat capacity ($\simeq$2020)
k	$9.83e^{-\frac{3}{2}T}$	(W m^{-1} K^{-1})	Thermal conductivity
k_0	9.83	(W m^{-1} K^{-1})	Conductivity prefactor
T^*	263.15	(K)	Transition temperature
n	3	(-)	Rheological exponent
A_0	3.50×10^{-25}	(Pa^{-n} s^{-1})	Ice softness prefactor
u_s	3.17×10^{-8}	(m s^{-1})	Surface velocity (= 1 m yr^{-1})
H	1000	(m)	Ice thickness scale
p_0	4.49×10^4	(Pa)	Dynamic ice pressure

[a]The temperature T is nondimensional, T/T^*.

where the horizontal and vertical components of velocity vector are $\boldsymbol{u} = (u, w)$. In these equations, there are two dimensionless groups, the Péclet number $\mathtt{Pe}$, the ratio of advection to diffusion,

$$\mathtt{Pe} = \frac{\rho c_p u_s H}{k_0},$$

and, the Brinkman number $\mathtt{Br}$, the ratio of viscous heat production to thermal diffusion,

$$\mathtt{Br} = \left(\frac{u_s}{A_0 H}\right)^{\frac{1}{n}} \frac{2u_s H}{k_0 T^*}.$$

Values from Table 1 give

$$\mathtt{Pe} \simeq 5.88, \quad \mathtt{Br} = 1.10 \times 10^{-3},$$

where we have used the typical value for specific heat capacity $c_p \simeq 2020$ J kg^{-1} K^{-1} to compute the Péclet number. We find that $\mathtt{Pe}$ is larger than unity indicating that advection dominates diffusion. The Brinkman number, however, is small, which is due to the slow horizontal velocity. This means that the effects of viscous heating are negligible and, therefore, we set $\mathtt{Br} = 0$ in our calculations.

2.3. Boundary Conditions

The boundary conditions for the temperature and ice flow are shown on the model valley schematic, Figure 5. The temperature at the surface is fixed at

$$T = \hat{T}_s \quad \text{on} \quad z = 1 \quad \text{with} \quad \hat{T}_s = \frac{T_m - 30}{T^*} = 0.92.$$

where −30°C is a representative value for the Gamburtsev Subglacial Mountains [*Comiso*, 2000; *Le Brocq et al.*, 2010]. Along the bottom boundary $z = b(x)$, we fix the temperature at the melting point, which is written nondimensionally as

$$T = \hat{T}_m \quad \text{on} \quad z = b \quad \text{with} \quad \hat{T}_m = \frac{T_m}{T^*} = 1.04.$$

We prefer this boundary condition to a geothermal heat flux because the sharp corner could lead to a large layer of temperate ice at the bottom of the domain. The induced melt rate would draw down the ice flow trajectories in the basal region. Moreover, this boundary condition is unlikely to affect the size and dimension of eddies.

For the flow boundary conditions, the horizontal velocity profile

$$u = 1 - (1 - z)^4 \tag{11}$$

is prescribed along the left boundary. This profile is the normalized analytical solution to the isothermal equations [*Nye*, 1952; *Fowler*, 2011; *Worster*, 2014] subject to no-slip basal boundary conditions. The pressure field p within the ice is the deviation from hydrostatic pressure, which we set equal to zero at the outlet.

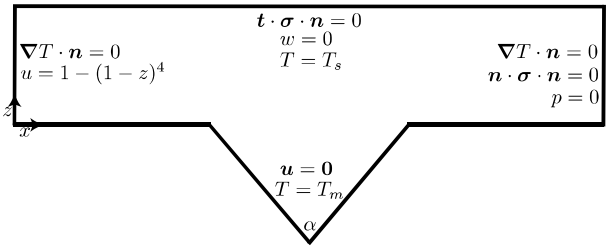

Figure 5. Model geometry including temperature and flow boundary conditions. All variables are nondimensional.

Along the upper boundary, we prescribe stress-free conditions on flow and do not include snow accumulation. The surface is steady and does not deform as the ice flows over the topography. While this is a commonly used approximation [*Nye*, 1952; *Raymond*, 1983; *Gudmundsson*, 1997], we have also run simulations where the surface evolves to a steady state. We find that the surface deflections are very small, and the structure of the Moffatt eddies is not altered. This is because Moffatt eddies are asymptotic features of a corner, and the bulk ice flow only acts as a far-field forcing.

3. Results

3.1. Structure of Two-Dimensional Eddies

Here we consider the flow of ice over the model valley. The valley opening angle is given by α. We consider three model valleys, which we refer to as wide ($\alpha = 143°$), intermediate ($\alpha = 113°$), and narrow ($\alpha = 90.0°$). For isothermal ice, the critical angle criteria determined by the similarity solution shows that Moffatt eddies should form in the intermediate and narrow valleys but not in the wide valley. Figures 6a–6c show numerical simulations of isothermal Glen's law ice. The background color is the vertical velocity w, and the blue arrows indicate the direction of flow. The streamlines show that a Moffatt eddy occurs in the narrow valley but not in the wide valley. The angle α for the intermediate case is close enough to the critical angle that the eddy is very small and not visible at this scale or streamline resolution. Thus, while the critical angle may predict an eddy in a valley, the resolution of our numerical simulations limits what valleys show Moffatt eddies.

We now simulate the flow of ice with a temperature-dependent rheology. The temperature field for the wide, intermediate, and narrow valleys is shown in Figures 7a–7c. The temperature profiles along the flow appear quite similar between the three cases, and the only major difference is that as the valley narrows more warm ice is trapped at the base. These temperature fields then affect the flow of ice in each valley. In the wide valley, the warmer ice near the base allows the basal ice to flow faster. The ice flows through the valley and does

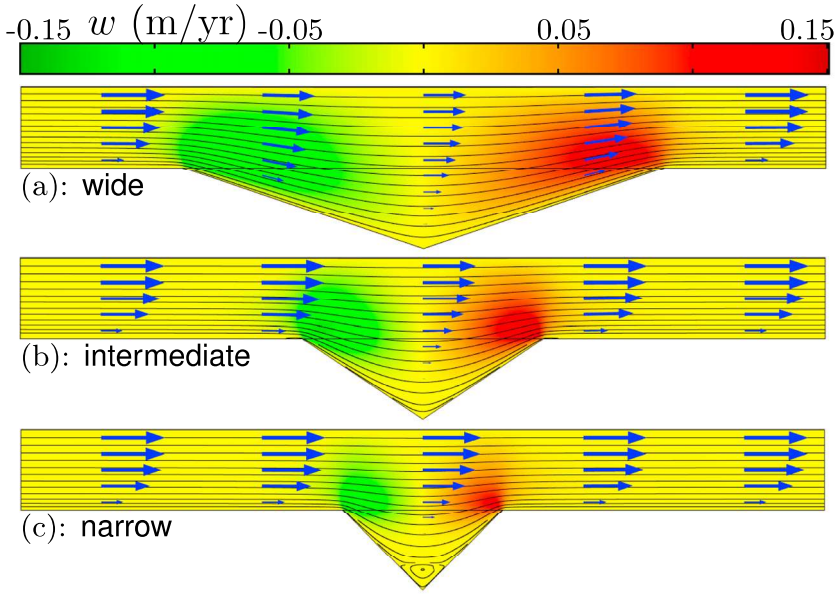

Figure 6. Isothermal ice flow simulations for the vertical velocity w (color) and horizontal velocity u (arrows) in a model valley with streamlines: (a) The wide valley angle exceeds critical angle for Moffatt eddy formation. (b) The intermediate valley is below the critical angle, but the eddy is too small for COMSOL to resolve. (c) A clear Moffatt eddy is visible in the narrow valley.

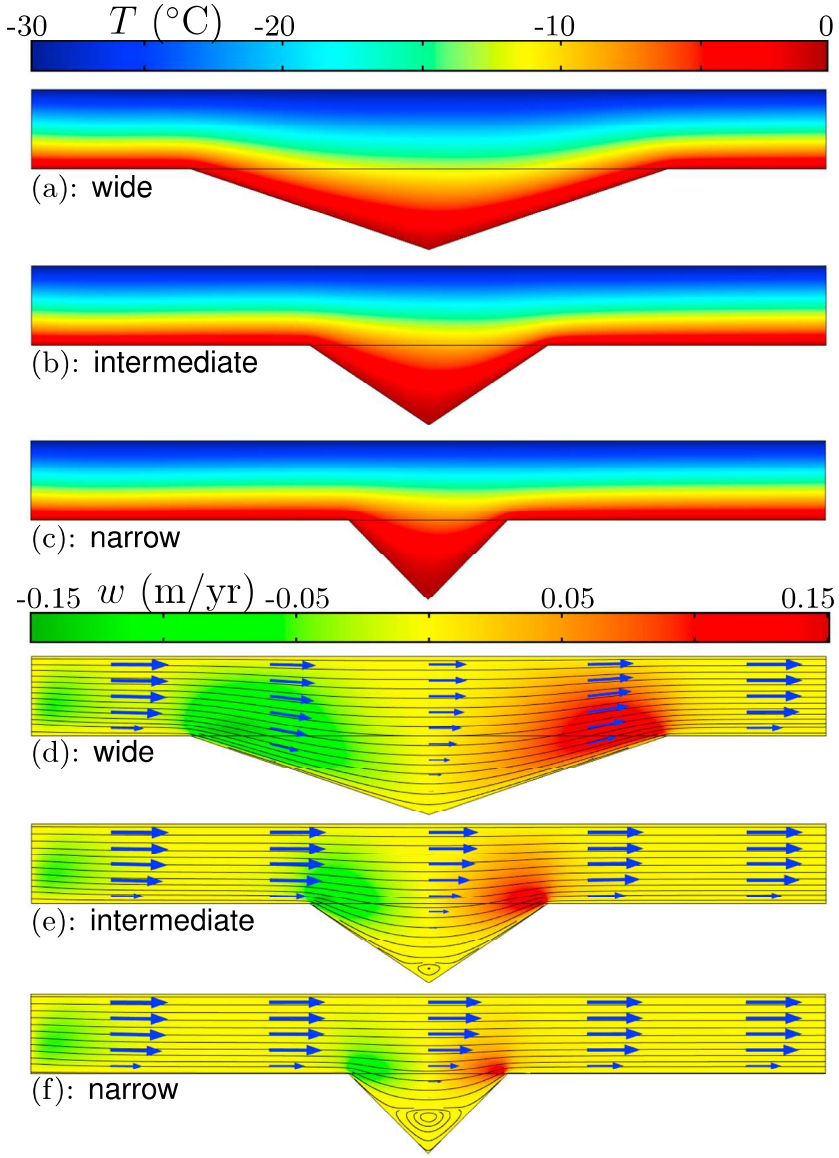

Figure 7. Vertical velocity w (color), horizontal velocity u (arrows), and temperature T in a model valley with streamlines: (a–c) Ice temperature varying between the surface temperature $T_s = -30°C$ and the melting temperature $T_m = 0°C$. (d) In the wide valley, no Moffatt eddy forms. (e) In the intermediate valley, the temperature gradient near the bed increases the size of the eddy and it becomes clearly visible. (f) The eddy in the narrow valley increases significantly due to the temperature gradient.

not form an eddy because the valley sidewalls are not steep enough. In both the intermediate and narrow valleys, however, there is a Moffatt eddy and it is larger than in the isothermal case. The temperature gradient introduces a new length scale into the problem that is not present in isothermal ice, leading to a variation in viscosity across the valley. The warmer ice near the bed is less viscous, which leads to an increase in the size of the Moffatt eddies.

3.1.1. Valley With Substructure

In subglacial valleys beneath ice sheets, the topography varies on a variety of length scales. To see the effect of substructure on Moffatt eddy shape and size, we superimpose smaller valleys onto the narrow model valley, cf. Figure 8. We first consider the isothermal case, Figure 8a, where eddies are present in every valley and their size increases with depth. Also, by comparing Figure 8a to 6c, we see that the substructure has a negligible effect on the size of the primary, deep eddy. In the temperature-dependent case, Figure 8b, the eddies from

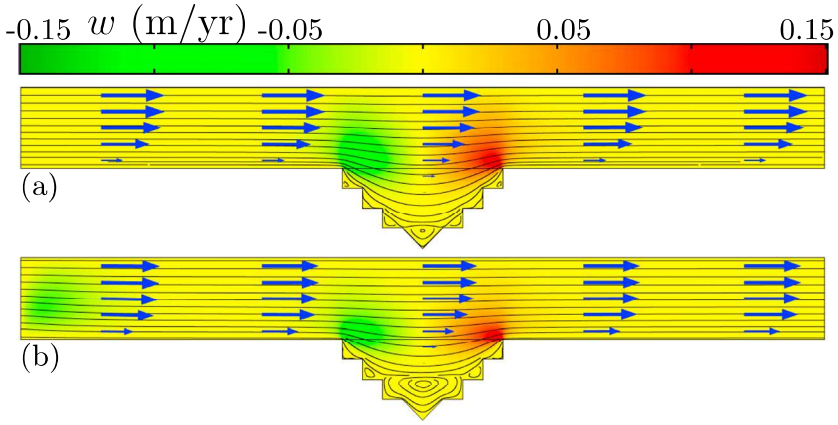

Figure 8. Vertical velocity *w* (color), horizontal velocity *u* (arrows), and streamlines shown in a sawtooth valley with small-scale topographic variation. The wedge angle is equivalent to the narrow valley in Figures 6 and 7. (a) In the isothermal case, Moffatt eddies form in each of the smaller valleys and a primary eddy forms in the valley bottom. (b) With a temperature-dependent viscosity, the lower eddies amalgamate and form a large eddy that follows the topography.

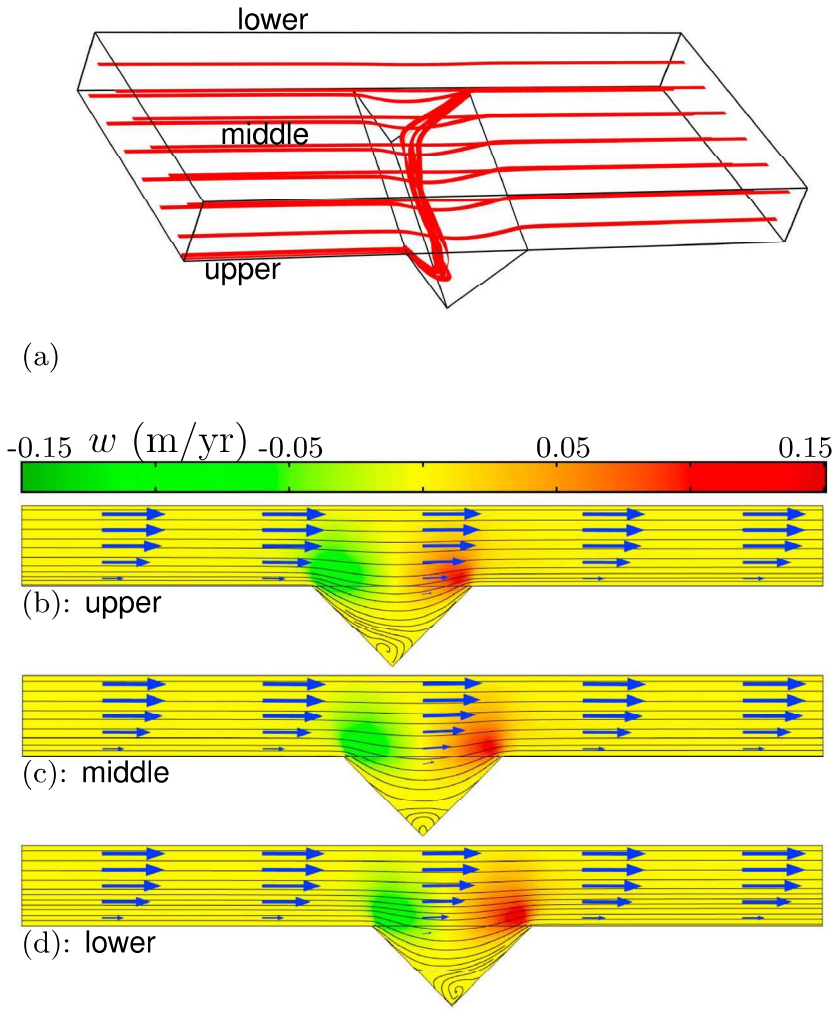

Figure 9. The vertical velocity *w* (color), horizontal velocity *u* (arrows), and streamlines in isothermal ice over an oblique valley forms three-dimensional eddies: (a) The red streamlines show a mean flow down the valley. (b–d) The evolution of basal eddies. The downstream evolution is different from the two-dimensional flow shown in Figure 6c.

the primary valley and the two adjacent valleys amalgamate and form a larger primary eddy that follows the topography.

3.2. Three-Dimensional Eddies

In both the similarity solution and the finite element computations, we consider only two-dimensional valley configurations. These configurations are logically equivalent to very wide three-dimensional valleys, where the flow is exactly perpendicular to the valley. We now consider a valley configuration that is fully three dimensional: flow across an oblique valley, cf. Figure 9a. For simplicity, we consider isothermal ice with stress-free sidewalls and surface as well as a no-slip condition along the bed. The inlet condition is the same prescribed flow profile, equation (11), and we apply zero fluid pressure with respect to hydrostatic at the outlet. The results of our numerical simulation are shown in Figure 9.

The streamlines show a significant fluid transport down the valley. This transport affects the character of the eddies at the base of the valley. In the upper part of the oblique valley, i.e., closest to the inlet, an eddy is formed but it is asymmetric and its core is elevated from the corner and shifted toward the inlet; see Figure 9b. A slice taken along the midplane shows a symmetrical eddy feature that is disturbed by the out-of-plane flow; see Figure 9c. The lower part of the valley, Figure 9b, is exactly antisymmetrical to the upper part of the oblique valley, and the eddy is displaced toward the outlet.

These results show that the angle between the flow and the valley orientation is important in describing the character of the eddies formed at the base of the ice sheet. In this paper, we principally consider the case of orthogonal flow over a uniform (or symmetric) valley because we are able to build up intuition and determine the critical angles for Moffatt eddy formation. The results for the oblique valley show that the transverse flow strongly influences the character of the eddies that form, which is consistent with the analysis of three-dimensional corner eddies described in the fluid mechanics literature [*Tokuda*, 1972; *Sano and Hashimoto*, 1980; *Scott*, 2013].

4. Discussion

Here we run the model simulations over radar-determined topography from the Gamburtsev Subglacial Mountains and compare the results to radar data.

4.1. Gamburtsev Radar Data

A location in Antarctica with deep valleys and radar data is the Gamburtsev Subglacial Mountains in central East Antarctica. The Gamburtsevs are a large mountain range (~750 km × 250 km) with steep relief typical of an alpine glacier system [*Creyts et al.*, 2014]. A digital elevation model of the Gamburtsev Subglacial Mountains is shown in Figure 10a. Generally thought to be the nucleation site for the East Antarctic Ice Sheet, the Gamburtsev topography arises from uplift that predates complete glaciation [*Bo et al.*, 2009; *Ferraccioli et al.*, 2011; *Rose et al.*, 2013]. The stark, well-preserved nature of the subglacial features indicates low rates of basal erosion [*Cox et al.*, 2010]. The combination of preserved topography relative to the location of Dome A results in ice flow oblique to valley orientation [*Creyts et al.*, 2014] and, therefore, makes valleys susceptible to Moffatt eddies.

A grid of ice-penetrating radar data was collected during the international polar year [*Bell and othes*, 2011]. Figure 10b shows the bed topography and ice surface elevation along the radar line in the Gamburtsevs. In Figure 10c, we compute the local bed angle and compare this angle with the critical slope necessary to develop Moffatt eddies determined by the similarity solution (equation (8) and Figure 4). The bed slope angles are greater than the critical angle in several places along this radar line. We choose the area around Latitude −81.7° along the radar line as a representative location to run numerical simulations based on the fact that there is a deep, steep valley, and the flow direction is nearly transverse to the valley orientation. The radar is shown in Figure 11c. The bed is clear, and we use the horizontally smoothed location of maximum gradient in radar return [*Wolovick et al.*, 2013]

4.2. Moffatt Eddies in Gamburtsevs Subglacial Valleys

Figure 11 shows numerical simulations of the governing conservation equations over the radar line from the Gamburtsev Subglacial Mountains. Figure 11a shows the steady state nondimensional temperature field. In the mountains the temperature is near the melting point, while in the center of the ice sheet, the temperature drops almost linearly. In Figure 11b, we show the computed streamlines for the flow, the horizontal velocity u (arrows), and the vertical velocity w (color). The velocity field is coupled to the temperature field through the

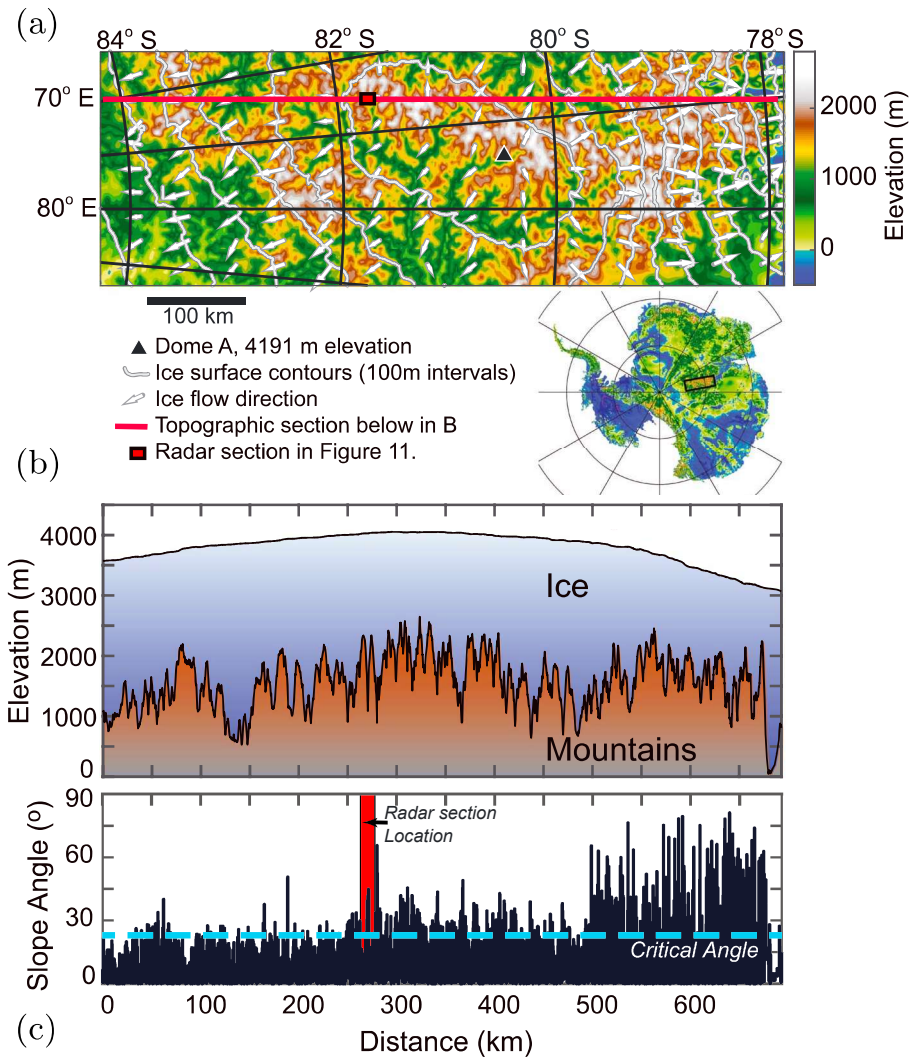

Figure 10. Gamburtsev Subglacial Mountains: (a) bed elevation digital elevation model with ice surface contours (ICEsat) [*Zwally et al.*, 2014] and ice velocity arrows. The red line shows radar line shown in Figure 10b, and black rectangle outlines the radar section for Figure 11 (adapted from *Creyts et al.* [2014]). (b) Bed and ice surface elevations along the red radar line from Figure 10a. (c) Bed slope angles (black) showing the critical angle for Moffatt eddies in blue and location of radar in Figure 11.

rheology, equation (10). In Figure 11c we plot the radargram showing the basal topography. Note that the flow is from right to left. From the streamlines, a Moffatt eddy can be seen in the deepest valley. An enlargement showing the vertical structure of the horizontal velocity of the eddy is shown in Figure 12, where we plot the velocity as a function of height.

A representative height scale for eddies is twice the distance between the two stagnation points; thus, Figure 12 shows that the eddy is about 200 m tall. The velocity of the ice within these eddies is extremely small. For a surface velocity of $u_s = 3.17 \times 10^{-8}$ m s^{-1}, the fastest flowing part of the eddy is moving at less than $u_e \sim 10^{-13}$ m s^{-1} or about 10 μm/yr.

The Moffatt eddy shown in Figures 11 and 12 is a steady state feature; however, we can think of a characteristic residence time for the ice in the eddy as the time for the ice in the outermost streamline to make a single full revolution. A scaling estimate for this characteristic residence time, t_r, is the height of the eddy $h \approx 200$ m divided by the maximum velocity $u_e \approx 10^{-5}$ m yr^{-1} in the eddy,

$$t_r \sim \frac{h}{u_e} \sim 2 \times 10^7 \text{ years.}$$

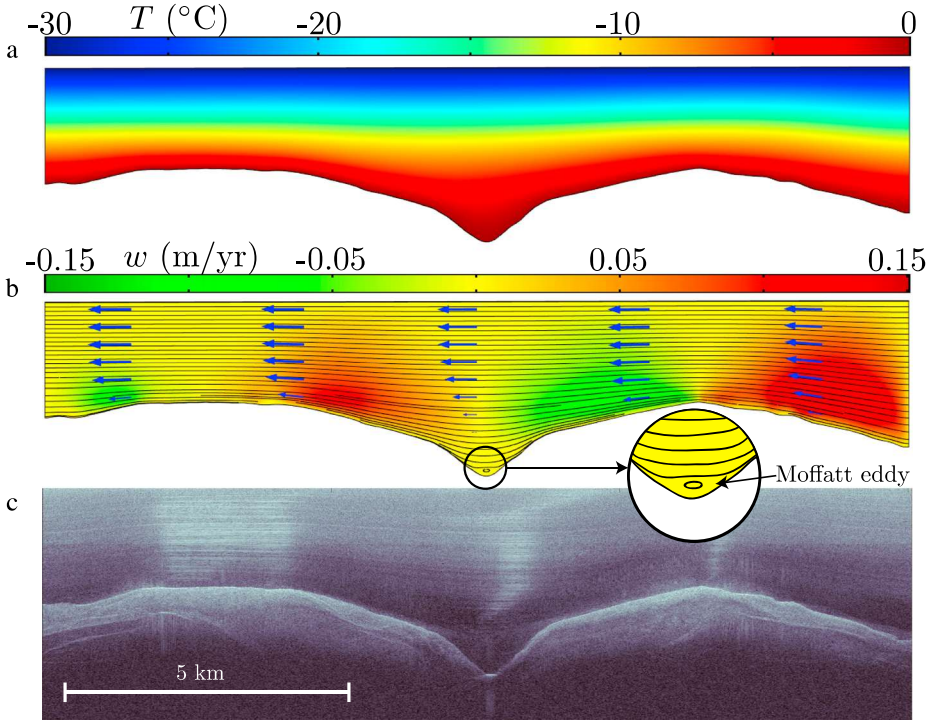

Figure 11. Simulation results for the vertical velocity w (color), horizontal velocity u (arrows), and temperature T over the radar line in the Gamburtsev Subglacial Mountains: (a) Temperature field. (b) Ice flow using the temperature-dependent rheology with streamlines showing the Moffatt eddy in the bottom of the valley. (c) Basal radargram matched to the computation domain. A bright spot that is potentially a small lake is visible at the bottom of the deep valley.

This timescale indicates that these eddies rotate very slowly compared to ice growth and decay. Thus, a change in surface boundary conditions through glacial cycles ($\sim 10^5$ years) should affect the development and rotation of an eddy. We can estimate a thermal diffusion timescale as

$$t_d \sim \frac{\rho c_p H^2}{k} \sim 3 \times 10^4 \text{ years},$$

which indicates that there is sufficient time for temperature changes to diffuse through the ice and influence eddy dynamics. The fact that $t_r \gg t_d$ suggests that eddies can form or dissipate due to changes in surface conditions on glacial timescales before making a complete rotation.

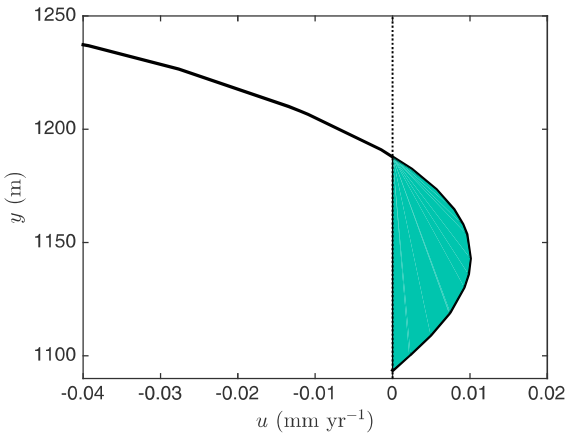

Figure 12. Eddy in Figure 11b: horizontal velocity with height from the bottom of the valley. The bottom half of the eddy is shown as the region of positive flow. Doubling the distance between the two stagnation points shows that eddy is on the order of 200 m tall.

4.3. Gamburtsev Ice Flow Structures and Radar

Our numerical simulations over topography on the radar line allow us to make direct comparisons between the simulations and radargrams. In particular, these numerical simulations show a Moffatt eddy forming in the central, deep valley. Here we compare the radar data in Figure 11c to the simulations in Figure 11b. Near the surface of the ice sheet, the radar clearly picks up the stratigraphic layers left by snow deposition. These layers advect with the flow of ice following streamlines. Ideally, these stratigraphic layers would be visible directly to the bed and eddies would be visible as disturbances to the layers, potentially encoding folded layering. At depth, however, the radar return signal is very weak and the radargram is dark. The ice appears homogeneous, and the layering is indistinct, which is consistent with nearly stagnant ice. At the bottom of the valley, there is an anomalously bright spot, which could be interpreted as a small lake [*Wolovick et al.*, 2013; *Creyts et al.*, 2014]. Neither the formation of this small lake nor the variation in basal slip over the lake is captured in our numerical simulations: we assume a no-slip boundary condition along the entire basal boundary and neglect the generation of heat within the ice and at the interface between the ice and basal sediments. We leave questions relating to the possible effects of localized slip arising from a subglacial lake for future work.

Here we describe the aspects of the radar data that confound the interpretation of the basal zone. Figure 11c shows that the clarity of the radar diminishes near the bed, a result of attenuation within the ice sheet [*Bogorodsky et al.*, 1983]. Below a critical depth there is a region called the "echo-free zone" (EFZ), which is potentially caused by variation in dielectric properties, ice crystal fabric, and heat content [*Annan*, 2008; *Drews et al.*, 2009]. The ice eddies shown in Figure 11 contribute to ice fabric reorganization and homogenization of heat content near the bed, potentially enhancing the EFZ.

Although subglacial valleys are locations of thick, potentially very old ice, the basal disturbances we show here indicate that subglacial valleys are likely unsuitable places to drill for long climate record ice cores. While several mechanisms have been used to explain the folding found in GRIP, GISP2, and NEEM [e.g., *Grootes et al.*, 1993; *Alley et al.*, 1997; *Dahl-Jensen et al.*, 2013], there is no a priori metric based on ice flow or topography to determine whether a location is suitable for ice core drilling. Here we show that Moffatt eddies result in folding and overturning. We describe a metric based on basal topography to differentiate between locations that may be susceptible to eddies and locations that are likely free of eddies. By calculating the basal slope from a digital elevation model, locations adjacent to slopes much greater than 23° can be ruled out as suitable locations to look for very old ice to be used for climate interpretations [*Fischer et al.*, 2013].

If an ice core is drilled in a deep subglacial valley, it would be important to know the size of the basal Moffatt eddy. A feature of the similarity solution from equation (7) is that there is no inherent governing length scale. The eddies are self-similar, and therefore, the height of the eddy cannot be determined from this analysis. In the basal topography, however, there are two dominant length scales: the depth of the valley and basal radius of curvature. The presence of these externally imposed length scales represents a breakdown of the similarity solution, i.e., the solution breaks down on the scale of the radius of curvature at the base of the valley [*Moffatt and Duffy*, 1980]. Figure 11b shows that both the basal curvature and the depth of the valley are important. For the temperature-dependent eddies, Figure 6 shows that the length scale over which the temperature gradient decays is also important in dictating the size of the eddies.

5. Conclusions

Motivated by complex flow and folding deep in the ice sheet, we have examined whether Moffatt eddies form in subglacial valleys. The eddies form deep in the corner, where the flow takes on a simple form. As a function of the rheological exponent n we have derived the critical valley angle for Moffatt eddy formation. We then examine numerical simulations of flow over model valleys and show that including the effects of temperature in the rheology lead to larger eddies. We use the critical angle determined by the similarity solution to find locations where Moffatt eddies may exist in the Antarctic Ice Sheet. Many valleys in the Gamburtsev Subglacial Mountains meet the criteria. These locations form the basis for our numerical simulations, where we run ice flow models over topography inferred by radar. Our simulations show Moffatt eddies in the subglacial valleys.

The velocity of the ice is very slow in these deep subglacial Moffatt eddies, leading to largely stagnant ice. This stagnation is similar to what would occur in a fluid with a yield stress flowing over undulatory terrain, where there would be yielded fluid flowing over plugged fluid in the troughs. This has important consequences for glacier motion over mountain ranges and overdeepenings, where the glacial ice can become stuck in the deep valley and modulate the surface velocity [*Gudmundsson*, 1997].

The comparison between the numerical simulations and radar data is inconclusive. There are features that are suggestive of Moffatt eddies, but ice attenuation due to the depth of the eddies conceals necessary details. Additional focused analyses are required to understand the deep ice radargrams and whether they contain Moffatt eddies. A simple metric that can be used to locate valleys that are potentially susceptible to subglacial Moffatt eddies is to compute the basal slopes based on a digital elevation model and find locations adjacent to slope angles greater than 23°. These would be the same regions to avoid in drilling for the oldest ice as the presence of basal eddies would inhibit past climate reconstructions of ice cores drilled in steep subglacial valleys.

Moffatt eddies are one type of deep ice stratigraphic disturbances, and these features require further study. There are several open avenues to explore on the fluid physics of Moffatt eddies in subglacial valleys. We plan to analyze the effect of a sliding law on the character of the eddies. We hope to map the disappearance of eddies with the addition of slip in an isothermal fluid as well as describe the mechanism by which they form in a fluid with a temperature-dependent viscosity and free-slip conditions along the bed. With a sliding law in place, we can incorporate features such as subglacial hydrology, which is known to be important in the Gamburtsevs [*Bell and othes*, 2011; *Wolovick et al.*, 2013; *Creyts et al.*, 2014].

The surface temperature, snowfall rate, and ice thickness are coupled to climate so that the heat flux through the ice is modulated on glacial-interglacial timescales. The waxing and waning of the ice sheet with climate also leads to changes in the strength of the near-bed ice as well as the slip condition along the bed. With a change in basal boundary conditions, the locations that potentially form eddies can switch from recirculating flow to having a simple shear profile. The change in flow means that the overturned layers of the eddies could be advected out of the valleys. Furthermore, we show in the case of complex three-dimensional topography that eddies move along and out of deep valleys. The movement of eddies downstream would then contaminate potential ice core drilling sites. Thus, deep ice cores require an understanding of eddies and how they generate basal disturbances over glacial-interglacial timescales.

Acknowledgments
We would like to thank Thibaut Perol, Jim Rice, and Grae Worster for insightful conversations as well as Sam Pegler, an anonymous reviewer, and the Associate Editor Olga Sergienko for constructive comments. Also, we acknowledge Mike Wolovick, Nick Frearson, and CReSIS for help with radar data and Antarctica's Gamburtsev Province study for the data. This research is supported by the U.S. NSF Graduate Research Fellowship under grant DGE1144152 (CRM), the U.S. NSF Polar Program grant PP1643970 (TTC), and the NASA Cryosphere grant NNX14AH79G (TTC). The radar data for Figure 10 can be obtained at ftp://data.cresis.ku.edu/data/rds/. Representative COMSOL and MATLAB simulation files can be obtained by request by e-mail to the corresponding author.

References

Acheson, D. (1990), *Elementary Fluid Dynamics*, Oxford Univ. Press, New York.
Alley, R. B., A. J. Gow, D. A. Meese, J. J. Fitzpatrick, E. D. Waddington, and J. F. Bolzan (1997), Grain-scale processes, folding, and stratigraphic disturbance in the GISP2 ice core, *J. Geophys. Res.*, *102*(C12), 26,819–26,830, doi:10.1029/96JC03836.
Annan, A. P. (2008), Electromagnetic principles of ground penetrating radar, in *Ground penetrating radar: theory and applications*, edited by H. M. Jol, pp. 3–40, Elsevier, Netherlands, AMS.
Bell, R. E., et al. (2011), Widespread persistent thickening of the East Antarctic Ice Sheet by freezing from the base, *Science*, *331*(6024), 1592–1595, doi:10.1126/science.1200109.
Bo, S., M. J. Siegert, S. M. Mudd, D. Sugden, S. Fujita, C. Xiangbin, J. Yunyun, T. Xueyuan, and L. Yuansheng (2009), The Gamburtsev mountains and the origin and early evolution of the Antarctic Ice Sheet, *Nature*, *459*(7247), 690–693, doi:10.1038/nature08024.
Bogorodsky, V., G. Bentley, and P. Gudmansen (1983), *Radioglaciology*, D. Reidel Publ. Co., Dordrecht, Netherlands.
Budd, W. F., P. L. Keage, and N. A. Blundy (1979), Empirical studies of ice sliding, *J. Glaciol.*, *23*, 157–170, doi:10.3198/1979JoG23-89-157-170.
Comiso, J. C. (2000), Variability and trends in Antarctic surface temperatures from in situ and satellite infrared measurements, *J. Clim.*, *13*(10), 1674–1696, doi:10.1175/1520-0442(2000)013<1674:vatias>2.0.co;2.
COMSOL (2006), *COMSOL Multiphysics: Version 4.3*, COMSOL, Stockholm, Sweden.
Cox, S. E., S. N. Thomson, P. W. Reiners, S. R. Hemming, and T. van de Flierdt (2010), Extremely low long-term erosion rates around the Gamburtsev Mountains in interior East Antarctica, *Geophys. Res. Lett.*, *37*, L22307, doi:10.1029/2010GL045106.
Creyts, T. T., et al. (2014), Freezing of ridges and water networks preserves the Gamburtsev Subglacial Mountains for millions of years, *Geophys. Res. Lett.*, *41*, 8114–8122, doi:10.1002/2014GL061491.
Cuffey, K. M., and W. S. B. Paterson (2010), *The Physics of Glaciers* 4th edn, Elsevier, Burlington, Mass.
Dahl-Jensen, D., et al. (2013), Eemian interglacial reconstructed from a Greenland folded ice core, *Nature*, *493*, 489–494, doi:10.1038/nature11789.
Drews, R., O. Eisen, I. Weikusat, S. Kipfstuhl, A. Lambrecht, D. Steinhage, F. Wilhelms, and H. Miller (2009), Layer disturbances and the radio-echo free zone in ice sheets, *Cryosphere*, *3*(2), 195–203, doi:10.5194/tc-3-195-2009.
Durham, W. B., S. H. Kirby, and L. A. Stern (1997), Creep of water ices at planetary conditions: A compilation, *J. Geophys. Res.*, *102*(E7), 16,293–16,302, doi:10.1029/97JE00916.
Fenner, R. T. (1975), On local solutions to non-Newtonian slow viscous flows, *Int. J. Non Linear Mech.*, *10*, 207–214, doi:10.1016/0020-7462(75)90012-8.
Ferraccioli, F., C. A. Finn, T. A. Jordan, R. E. Bell, L. M. Anderson, and D. Damaske (2011), East antarctic rifting triggers uplift of the Gamburtsev mountains, *Nature*, *479*, 388–392, doi:10.1038/nature10566.
Fischer, H., et al. (2013), Where to find 1.5 million year old ice for the IPICS "oldest ice" ice core, *Clim. Past*, *9*, 2489–2505, doi:10.5194/cp-9-2489-2013.
Fowler, A. (2011), *Mathematical Geoscience*, vol. 36, Springer Science & Business Media, London, U. K.
Glen, J. W. (1955), The creep of polycrystalline ice, *Proc. R. Soc. London, Ser. A*, *228*(1175), 519–538, doi:10.1098/rspa.1955.0066.
Goldsby, D., and D. Kohlstedt (2001), Superplastic deformation of ice: Experimental observations, *J. Geophys. Res.*, *106*, 11,017–11,030, doi:10.1029/2000JB900336.
Grootes, P. M., M. Stuiver, J. W. C. White, S. Johnsen, and J. Jouzel (1993), Comparison of oxygen isotope records from the GISP2 and GRIP Greenland ice cores, *Nature*, *366*, 552–554, doi:10.1038/366552a0.

Gudmundsson, G. H. (1997), Basal-flow characteristics of a non-linear flow sliding frictionless over strongly undulating bedrock, *J. Glaciol.*, *43*(143), 80–89, doi:10.1017/S0022143000002835.
Henriksen, P., and O. Hassager (1989), Corner flow of power law fluid, *J. Rheology*, *33*(6), 865–879, doi:10.1122/1.550039.
Hindmarsh, R. C. A. (2004), A numerical comparison of approximations to the Stokes equations used in ice sheet and glacier modeling, *J. Geophys. Res.*, *109*, F01012, doi:10.1029/2003JF000065.
Hudleston, P. J. (1976), Recumbent folding in the base of the barnes ice cap, Baffin Island, Northwest Territories, Canada, *Geol. Soc. Am. Bull.*, *87*(12), 1684–1692.
Hudleston, P. J., and O. Stephansson (1973), Layer shortening and fold-shape development in the buckling of single layers, *Tectonophysics*, *17*(4), 299–321.
Hutchinson, J. W. (1968), Singular behavior at the end of a tensile crack in a hardening material, *J. Mech. Phys. Solids*, *16*, 18–31, doi:10.1016/0022-5096(68)90014-8.
Hutter, K., and V. O. S. Olunloyo (1980), On the distribution of stress and velocity in an ice strip, which is partly sliding over and partly adhering to its bed, by using a Newtonian viscous approximation, *Proc. R. Soc. London, Ser. A*, *373*(1754), 385–403, doi:10.1098/rspa.1980.0155.
Jacobel, R. W., and S. M. Hodge (1995), Radar internal layers from the Greenland summit, *Geophys. Res. Lett.*, *22*(5), 587–590.
Le Brocq, A. M., A. J. Payne, and A. Vieli (2010), An improved antarctic dataset for high resolution numerical ice sheet models (ALBMAP v1), *Earth Syst. Sci. Data*, *2*(2), 247–260, doi:10.5194/essd-2-247-2010.
Lliboutry, L. (1968), General theory of subglacial cavitation and sliding of temperate glaciers, *J. Glaciol.*, *7*, 21–58, doi:10.1017/S0022143000020396.
McMeeking, R. M., and R. E. Johnson (1986), On the mechanics of surging glaciers, *J. Glaciol.*, *32*(110), 120–132, doi:10.3198/1986JoG32-110-120-132.
Moffatt, H. K. (1964a), Viscous and resistive eddies near a sharp corner, *J. Fluid Mech.*, *18*, 1–18, doi:10.1017/S0022112064000015.
Moffatt, H. K. (1964b), Viscous eddies near a sharp corner (viscous eddy behavior near sharp corner, considering outer boundary conditions and stream function), *Archiwum Mechaniki Stosowanej*, *16*(2), 365–372.
Moffatt, H. K., and B. R. Duffy (1980), Local similarity solutions and their limitations, *J. Fluid Mech.*, *96*(2), 299–313, doi:10.1017/S0022112080002133.
Nye, J. F. (1952), The mechanics of glacier flow, *J. Glaciol.*, *2*(12), 82–93, doi:10.3198/1952JoG2-12-82-93.
Raymond, C. F. (1983), Deformation in the vicinity of ice divides, *J. Glaciol.*, *29*(103), 357–373, doi:10.3198/1983JoG29-103-357-373.
Rignot, E., J. Mouginot, and B. Scheuchl (2011), Ice flow of the Antarctic ice sheet, *Science*, *333*(6048), 1427–1430, doi:10.1126/science.1208336.
Rose, K. C., F. Ferraccioli, S. S. R. Jamieson, R. E. Bell, H. Corr, T. T. Creyts, D. Braaten, T. A. Jordan, P. T. Fretwell, and D. Damaske (2013), Early east Antarctic Ice Sheet growth recorded in the landscape of the Gamburtsev Subglacial Mountains, *Earth Planet. Sci. Lett.*, *375*, 1–12, doi:10.1016/j.epsl.2013.03.053.
Sano, O., and H. Hashimoto (1980), Three-dimensional moffatt-type eddies due to a stokeslet in a corner, *J. Phys. Soc. Jpn.*, *48*(5), 1763–1768, doi:10.1143/JPSJ.48.1763.
Schoof, C. (2005), The effect of cavitation on glacier sliding, *Proc. R. Soc. London, Ser. A*, *461*(2055), 609–627, doi:10.1098/rspa.2004.1350.
Scott, J. F. (2013), Moffatt-type flows in a trihedral cone, *J. Fluid Mech.*, *725*, 446–461, doi:10.1017/jfm.2013.180.
Taneda, S. (1979), Visualization of separating stokes flows, *J. Phys. Soc. Jpn*, *46*(6), 1935–1942, doi:10.1143/JPSJ.46.1935.
Tokuda, N. (1972), Viscous flow near a corner in three dimensions, *J. Fluid Mech.*, *53*(1), 129–148, doi:10.1017/S0022112072000072.
Van Liefferinge, B., and F. Pattyn (2013), Using ice-flow models to evaluate potential sites of million year-old ice in Antarctica, *Clim. Past*, *9*(5), 2335, doi:10.5194/cp-9-2335-2013.
Waddington, E. D., J. F. Bolzan, and R. B. Alley (2001), Potential for stratigraphic folding near ice-sheet centers, *J. Glaciol.*, *47*(159), 639–648, doi:10.3189/172756501781831756.
Weertman, J. (1957), On the sliding of glaciers, *J. Glaciol.*, *3*(21), 33–38, doi:10.3198/1957JoG3-21-33-38.
Weertman, J. (1976), Sliding-no sliding zone effect and age determination of ice cores, *Quat. Res.*, *6*(2), 203–207, doi:10.1016/0033-5894(76)90050-8.
Whillans, I. M., and K. C. Jezek (1987), Folding in the Greenland ice sheet, *J. Geophys. Res.*, *92*(B1), 485–493, doi:10.1029/JB092iB01p00485.
Wolovick, M. J., R. E. Bell, T. T. Creyts, and N. Frearson (2013), Identification and control of subglacial water networks under Dome A, Antarctica, *J. Geophys. Res. Earth Surf.*, *118*, 140–154, doi:10.1029/2012JF002555.
Wolovick, M. J., T. T. Creyts, W. R. Buck, and R. E. Bell (2014), Traveling slippery patches produce thickness-scale folds in ice sheets, *Geophys. Res. Lett.*, *41*, 8895–8901, doi:10.1002/2014GL062248.
Worster, M. G. (2014), Dynamics of marine ice sheets, *Procedia IUTAM*, *10*, 263–272, doi:10.1016/j.piutam.2014.01.022.
Zwally, H. J., R. Schutz, D. Hancock, and J. Dimarzio (2014), *GLAS/ICEsat I2 Antarctic and Greenland Ice Sheet Altimetry Data (HDF5), version 34*, Natl. Snow and Ice Data Cent., Boulder, Colo.